Monte Carlo evaluation of hypothetical long axial field-of-view PET scanner using GE Discovery MI PET front-end architecture

Ashok Tiwari[1,2], Michael Merrick[1,3], and Stephen A. Graves[1,3,4], John Sunderland[1,2,4] *

[1] Department of Radiology, University of Iowa Hospitals and Clinics, 200 Hawkins Dr., Iowa City, IA 52242, USA

[2] Department of Physics and Astronomy, University of Iowa, 203 Van Allen Hall, Iowa City, IA 52242, USA

[3] Department of Biomedical Engineering, University of Iowa, 5601 Seamans Center, Iowa City, IA 52242, USA

[4] Department of Radiation Oncology, University of Iowa Hospitals and Clinics, 200 Hawkins Dr., Iowa City, IA 52242, USA

Running title: MC evaluation of DMI PET scanners

* Author to whom correspondence should be addressed. Electronic mail: john-sunderland@uiowa.edu, Department of Radiology, University of Iowa Hospitals and Clinics, 200 Hawkins Dr., Iowa City, IA 52242, USA

Abstract

Purpose: The development of total-body PET scanners is of growing interest in the PET community. Investigation into the imaging properties of a hypothetical extended axial field-of-view (AFOV) GE Healthcare SiPM-based Discovery MI (DMI) system architecture has not yet been performed. In this work, we assessed its potential as a whole-body scanner using Monte Carlo simulations. The aim of this work was to (1) develop and validate a Monte Carlo model of a 4-ring scanner and (2) extend its AFOV up to 2 m to evaluate performance gain through NEMA-based evaluation.

This article has been accepted for publication and undergone full peer review but has not been through the copyediting, typesetting, pagination and proofreading process, which may lead to differences between this version and the Version of Record. Please cite this article as doi: 10.1002/mp.15422.

Methods: The DMI 4-ring geometry and its pulse digitization scheme were modeled within the GATE Monte Carlo platform using published literature. The GATE scanner model was validated by comparing results against published NEMA performance measurements. Following the validation of the 4-ring model, the model was extended to simulate 8, 20, 30, and 40-ring systems. Spatial resolution, sensitivity, NECR, and scatter fraction were characterized with modified NEMA NU-2 2018 standards; however, the image quality measurements were not acquired due to computational limitations. Spatial resolutions were simulated for all scanner ring configurations using point sources to examine the effects of parallax errors. NEMA count rates were estimated using a standard 70 cm scatter phantom and an extended version of scatter phantom of length 200 cm with (1-800) MBq of ^{18}F for all scanners. Sensitivity was evaluated using NEMA methods with a 70 cm standard and a 200 cm long line source.

Results: The average FWHM of the radial/tangential/axial spatial resolution reconstructed with filtered back-projection at 1 and 10 cm from the scanner center were 3.94/4.10/4.41 mm and 5.29/4.89/5.90 mm for the 4-ring scanner. Sensitivity was determined to be 14.86 cps/kBq at the center of the FOV for the 4-ring scanner using a 70 cm line source. Sensitivity enhancement up to 21-fold and 60-fold were observed for 1 m and 2 m AFOV scanners compared to 4-ring scanner using a 200 cm long line source. Spatial resolution simulations in a 2 m AFOV scanner suggest a maximum degradation of ~23.8% in the axial resolution compared to the 4-ring scanner. However, the transverse resolution was found to be relatively constant when increasing the axial acceptance angle up to ±70º. The peak NECR was 212.92 kcps at 22.70 kBq/mL with a scatter fraction of 38.9% for a 4-ring scanner with a 70 cm scatter phantom. Comparison of peak NECR using the 200 cm long scatter phantom relative to the 4-ring scanner resulted in a NECR gain of 15 for the 20-ring and 28 for the

40-ring geometry. Spatial resolution, sensitivity, and scatter fraction showed an agreement within ~7% compared with published measured values.

Conclusions: The 4-ring DMI scanner simulation was successfully validated against published NEMA measurements. Sensitivity and NECR performance of extended 1 and 2 meters AFOV scanners based upon the DMI architecture were subsequently simulated. Increases in sensitivity and count-rate performance are consistent with prior simulation studies utilizing extensions of the Siemens mCT architecture and published NEMA measurements with the uEXPLORER system.

Keywords: PET, extended axial field-of-view, GATE Monte Carlo, NEMA NU 2-2018, Discovery MI

1. INTRODUCTION

There has been a significant interest in developing long axial field-of-view (LAFOV) PET scanners to enhance the geometric sensitivity of PET systems. The latest standard geometry commercial silicon photomultiplier (SiPM)-based clinical PET scanners typically have an axial field-of-view (AFOV) of 15-30 cm.[1-3] However, several limitations are associated with a limited AFOV, such as low photon detection efficiency[4-7], longer scanning time, the requirement of higher radioactivity injections, and difficulty in large field of view parametric and pharmacokinetic PET imaging.[8-12] Significant efforts have been made recently developing a total-body and LAFOV PET scanner that can image the patient using only a single bed position in a relatively short scanning time with lower injected activity.[13,14] In addition, the LAFOV scanners can extend the imaging to multisystem diseases by implementation of multi-organ multi-parametric PET combining Standardized Uptake Value (SUV) PET with kinetic modeling[15-18], and even thorax breath-hold imaging.[19]

To date, a few platforms have been developed, including the uEXPLORER[13,20,21], PennPET EXPLORER[22,23], and the Siemens Biograph Vision Quadra.[14,24,25] The uEXPLORER uses the similar detector as the United Imaging Healthcare's uMI 550 and 780 PET/CT scanners, however the LYSO crystal depth is more by ~2 mm. In addition, the PennPET Explorer is based on the Philips detector technology and detector geometry used in the Vereos scanner.[6] The Biograph Vision Quadra uses the same technology as digital Biograph Vision 600 PET/CT system (Siemens Healthineers).[24] All these scanners use a modern SiPM technology instead of traditional photomultipliers. First human studies on the uEXPLORER total-body PET scanner have already been performed while utilizing substantially lower administered activity (~25 MBq) and a short total acquisition time of ~1 min.[7,26] The PennPET EXPLORER group recently reported their development of a whole-body imager currently with an active 64 cm AFOV and indicated that the optimal axial length of the scanner could be in the range of (1.0 -1.4 m).[22]

The scanner architecture of Phillips Vereos PET scanner[22,27] and United Imaging Healthcare's uMI scanner[13] have been studied for the total-body PET scanner design both through Monte Carlo simulation and downstream physical testing. Similarly, the front-end scanner architecture of Biograph Vision 600 PET/CT has been implemented in Biograph Vision Quadra.[14] Monte Carlo simulation of the Discovery STE PET/CT scanner and its reduced and extended AFOV has been performed using the SimSET toolkit.[28] In addition, Monte Carlo studies of the Siemens Biograph mCT scanner were performed in 2012 using the GATE (Geant4 Application for Tomographic Emission) simulation toolkit.[29] Their study suggested that the extended axial coverage of 2 m with 20 mm thick LSO crystals yields a relative performance gain of (25 – 31) times higher NECR.[29] In another simulation study, Surti et al. simulated imaging at activity levels as low as 1/20th of that typically injected for routine ^{18}F-FDG studies using the EGS4 code with a scanner AFOV of 72 cm.[30]

Monte Carlo simulations have been used for assessing the performance of hypothetical LAFOV PET systems adopted from existing clinical PET systems but with sparse detector geometries to reduce the manufacturing and purchasing cost of such scanners thus facilitating their wider clinical adoption. Specifically, Monte Carlo studies have been performed comparing the NEMA performance of existing clinical PET systems with compact detector configurations against those adapting sparse detector configurations with either (i) same detector ring diameter and AFOV but only half the detectors[31] or (ii) same detector ring diameter and number of detectors but spaced out to cover twice the original AFOV.[32-36] The validated Monte Carlo model proposed in this study could also be used in future to expand knowledge in this area for hypothetical sparse detector configurations based on commercial GE PET scanner geometries.

To our knowledge, the investigation into the imaging properties of a hypothetical extended axial field-of-view GE Healthcare Discovery MI (DMI) scanner system architecture has not been performed. This is of particular interest because the LYSO detector thickness in DMI is more than 20% longer than the aforementioned systems. The DMI PET scanner is currently available in 3, 4, and 5-ring configurations that provides a 15, 20, and 25 cm AFOV. In this study, our goal was to explore and understand the potential of the DMI architecture for a total-body scanner by looking at the performance gain with increasing AFOV through simulation. First, to validate our Monte Carlo model of the DMI detection system, we simulated the front-end architecture of the GE Discovery MI PET 4-ring scanner using the GATE toolkit and compared against published NEMA measurements from DMI 4 ring systems.[1] After validation, we gradually added the scanner rings to the AFOV up to 2 meters. NEMA performance results were obtained for the hypothetical extended AFOV scanners with several configurations, between 4 and 40 rings. The axial sensitivity, spatial resolution, count rates, scatter fraction, and Noise Equivalent Count Rates (NECR) were measured according to the modified NEMA protocols as implemented by Spencer et al.[13] using modified NEMA phantoms.

2. MATERIALS AND METHODS

2.1. Monte Carlo Simulations

The GEANT4 Application for Tomographic Emission (GATE) is a Monte Carlo toolkit for nuclear imaging[37-39], radiotherapy, and dosimetry.[40-43] GATE version 8.1 with Geant4 10.4.1[44] was used to model the Discovery MI scanner and simulate particle propagation. The physics list of *emstandard_opt4* was used in all simulations, as this model has previously been shown to be appropriate for medical applications involving electromagnetic effects.[45,46] This list includes all the relevant physical processes for photons and electrons interactions (i.e., photoelectric effect, Compton scattering, Rayleigh scattering, ionization, bremsstrahlung, multiple scattering, and positron annihilation). The decay of ^{18}F were simulated by β^{+} sources with energy spectra parametrized according to the Landolt-Börnstein tables.[37] Range production cuts were set to 0.1 mm for electrons and photons in the whole geometry. Variance reduction techniques were not used. The number of primary particles was adapted for all simulations according to the NEMA guidelines regarding activity and acquisition time. Optical processes of light emission and transport were not included in the simulations, as these processes substantially increase the simulation time.

2.2. Discovery MI 4-ring scanner geometry

The Discovery MI scanner used in this work is the latest generation of PET/CT scanners developed by GE Healthcare utilizing the silicon photomultiplier (SiPM) based technology.[1,47] The scanner system has been integrated with 64 slice x-ray computed tomography system and a 4-ring PET geometry with LightBurst digital detectors providing a 20 cm AFOV and a 70 cm transaxial field of view, i.e., the scanner bore diameter. Each ring consists of 34 detector modules, each containing 4 axial and 4 transaxial blocks, for a total of 544 detector blocks. Each detector block is 16 mm (transaxial) × 48 mm (axial) and contains a 4 (transaxial) × 9 (axial) crystal array, with crystals placed on three 3 × 2 arrays of SiPM detectors, for a total of 19,584 crystals and 9,792 SiPM channels. The SiPM signal readout electronics are implemented as an application-specific integrated circuit. The output energy is digitized by an external analog-to-digital converter (ADC) and the timing signal by an external time-to-digital converter. The size of each crystal used is 3.95 mm (transaxial) × 5.3 mm (axial) × 25 mm (depth), with several crystals connected to light guides that optimize light collection and improve sensitivity and resolution. The crystals themselves are radioactive due to the very long half-life, naturally occuring lutetium isotope ^{176}Lu that comprises 2.6% of natural lutetium.[48]

2.3. GATE Modelling of Discovery MI scanner

The cylindrical PET scanner architecture was defined by a set of hierarchically arranged elements with four different depth levels. First level was a detector module. Each module was repeated in a ring-like manner 34 times and each module was composed of an array of 4 (transaxial) x 4 (axial) blocks (second depth level). The blocks were divided into a grid of 4 (transaxial) x 9 (axial) array, this is the third level of the system. Each gird finally housed a LYSO crystal of size 3.95 x 5.3 x 25 mm^3(fourth level). GATE repeaters were utilized so that every crystal did not have to be added manually. The crystal was repeated 36 times in each block, 4 in the y-direction and 9 in the z-direction. The blocks were then repeated 4 times in y and z-direction inside the detector module. Since the crystals were already repeated in the block, and the block was repeated in its entirety, all the module sub-volumes accompanied the repeated module. The extended AFOV scanners for 8, 20, 30, and 40 rings were modeled by repeating the scanner module 8, 20, 30, and 40 times respectively, while keeping the other geometry the same. The total number of detector elements for the (4 - 40) ring consists of (19,584 - 195,840) LYSO crystals. In addition, the attenuating materials locating at the front face of the crystals were simulated (0.7 mm thick plastic polycarbonate, 0.1 mm thick metalized mylar and mylar window of 1.5 mm thickness) based on the information provided by the GE through private communication.

Scintillation photons were digitized in GATE using the *digitizer module*. The digitizer is composed of several signal processing operations that mimic the photon detection process. The signal processing chain start with adding the *hits* (individual photons interactions) into *pulses*, converting them into singles, and sorting them into final *coincidences*. Several parameters were defined along the digitizer chain, such as crystal energy resolution at 511 keV, timing resolution, lower and upper-level energy discriminators, and the coincidence window as tabulated in **Table 1**. However, for extended axial FOV scanners, the coincidence timing window was estimated based on the empirical formula available in the literature to account for the relatively large difference in maximum time-of-flight values between the direct and oblique lines of response.[29,49] The optimal coincidence timing window for extended AFOV scanners were calculated according to the equation:

$$\tau = \frac{FOV_{trans}\sqrt{1+(\tan(\alpha))^2}}{c} + 3\Delta t \tag{1}$$

where FOV_{trans} is the transaxial FOV (70 cm), α is the acceptance angle, Δt is the coincidence timing resolution (375 ps), and c is the speed of light in a vacuum. The acceptance angles for 4-, 8-, 20-, 30-, and 40-ring scanners are ±15º, ±30º, ±55º, ±65º, and ±70º respectively.

The simulated scanner deadtime, however, was heuristically and necessarily tuned to match the experimental count-rate measurements. The scanner's non-paralysable deadtime of 200 ns was found to mimic the measurements closely. In GATE digitizer the *setDepth* value of 2 was used based on the preliminary simulation results. In addition, the non-paralysable deadtime was applied on the singles before the coincidence sorter at the depth level of detector module. The coincidence policy was set to *takeAllGoods* for all simulations in the coincidence sorter settings as it is recommended for the single window method and to accept all possible coincidences within the geometric limits set by the scanner.[50]

2.3.1. Intrinsic Activity in LYSO crystals

Lutetium contains about ~2.6% of ^{176}Lu, which decays by β-emission (E_{max} 593 keV) with a cascade of three γ-ray emissions (88 keV, 202 keV, and 307 keV).[48,51] Using the simulated density of LYSO (7.11 gm/cm^3), molar mass ($Lu_{1.8}Y_{0.2}SiO_5$:Ce), and half-life of ^{176}Lu (3.6 x 10^{10} y)[52], an intrinsic detector activity of 268.85 Bq/mL was calculated. This isotope emits 88 keV, 202 keV, and 307 keV gammas and two betas (E_{max} 192 keV, 0.4% and E_{max} 593 keV, 99.6%).[48] The emitted gamma energies are outside the PET acquisition's energy window (425 – 625 keV). Decays of ^{176}Lu were included in Monte Carlo simulations. This intrinsic activity within the LYSO crystals was simulated as a ^{176}Lu ion source, which is the most accurate method to simulate the radioactive decay.[44] The intrinsic activity source encompassed the whole scanner, and the activity (ion source) was confined to the LYSO scintillation crystals.[53] To quantify the impact of intrinsic activities, scanner performance was simulated with and without intrinsic activities. The count rate curves for DMI 4-ring configuration with and without ^{176}Lu background intrinsic activities are generated for visual inspection, and the ratio of NECR with and without intrinsic activity is estimated. This ratio quantifies the factor by which the ^{176}Lu background degrades the emission data.

2.4. System Performance

The GATE model of the Discovery MI 4-ring scanner was validated by comparing the sensitivity, spatial resolution, and NECR results of the NEMA acceptance measurements performed by Hsu et al. at Stanford University.[1] Other measurement results are also available.[54,55] The NEMA sensitivity phantom, scatter phantom, and spatial resolution phantoms defined by NEMA NU 2-2018 protocols[56] were accurately modeled to measure the simulated DMI PET scanner performance. The tests outlined in these procedures have been mainly devised to provide a comprehensive description of typical clinical scanners' performance.

2.4.1. Spatial resolution

Monte Carlo modeling of spatial resolution measurements was performed according to the NEMA NU-2 2018 procedure using ^{18}F point sources. The point sources are capillary glass tubes of length 1mm, wall thickness of 0.4 mm, and internal diameter of 1 mm. The activity per source was 0.15 kBq, about ~190 kBq/cc for all point sources. Simulations using 4-ring scanner were performed with sources placed at 1 and 10 cm radial offset vertically from the center of the FOV to compare the simulation result with measurement data. In addition, to understand the effects of parallax error, spatial resolution was simulated with sources placed at 0, 1, 5, 10, 15, and 20 cm radial offset vertically from the center of the scanner FOV in air using all (4 - 40) scanner ring configurations. Simulation was performed such that the total coincidences were greater than 100,000 per point source. The simulation output data were reconstructed using the filter back projection (FBP) algorithm with a voxel size of 2 x 2 x 3.5 mm^3, without any smoothing, as specified in the NEMA procedure using the STIR[57] reconstruction platform. The full width at half maximum (FWHM) and full width at tenth maximum (FWTM) of the point source response function were evaluated by plotting one-dimensional response functions along with line profiles through the peak of the distribution of each point source using ImageJ.[58] System axial, tangential, and radial spatial resolutions were obtained as per NEMA requirement.[56]

2.4.2. Sensitivity

The NEMA PET Sensitivity Phantom was simulated to measure the sensitivity of the scanner. The purpose of this test is to measure the ability of the GATE DMI scanner system to detect the true coincidence events per second per unit of radioactivity in the FOV. The sensitivity phantom consists of five concentric aluminum tubes used to detect camera sensitivity in PET with all 700 mm long cylinders. The innermost polyethylene (density 0.96 g/cm^3) tube has a fillable volume with an internal diameter of 2 mm and wall thickness of 0.6 mm. All tubes were modeled in GATE for sensitivity measurements. Aluminum tubes (density 2.7 g/cm^3) were subsequently added one at a time for simulation. The decay of nuclides was simulated using the F-18 positron emission source, and decay correction was performed for subsequent simulations to mimic physical measurements. A standard 70 cm long line source with an outer and inner diameter of 3.2 mm and 2 mm was simulated for a line source insert for the 4 and 8-ring scanners. In addition, a 200 cm long cylindrical line source, in aluminum sleeves of varying thickness, with the same diameter was simulated in all scanner configurations (4, 8, 20, 30 and 40-ring) for sensitivity comparison. 4 MBq ^{18}F sources were used in all cases. The sensitivity phantoms were simulated for thirty seconds to minimize statistical uncertainty. Trues-only sensitivity was simulated by subtracting random events, and negligible scatter events from prompt coincidence events. All simulations had true counts of more than 100,000 coincidences. Random events were estimated using the singles rate method. For each added sleeve, the total number of true coincidences per slice was calculated using single-slice rebinning and normalized by source activity and total acquisition time. Sensitivity for each aluminum tube was computed, and the sensitivity without attenuation was determined by extrapolation to zero thickness.

2.4.3. Count rates, scatter fraction, and Noise Equivalent Count Rates

The NEMA scatter phantom is a right circular cylinder of a polyethylene material of density of 0.96 g/cm^3, with an outside diameter of 20.3 cm and length of 70 cm.[56] A line source is a hollow cylinder with an inner diameter of 3.2 mm. It is inserted in a hole of diameter 6.4 mm drilled at a radial offset of 45 mm parallel to the phantom's central axis. The material of the line source is also polyethylene. Two versions of scatter phantoms were simulated, one with the phantom of length of 70 cm, as recommended by NEMA, and the other with a length of 200 cm for count rates, scatter fraction (SF) and the NECR evaluation of longer than 8-ring PET geometries. Data were acquired using sufficient particles such that statistical uncertainties in simulations are less than 2%. Simulations were performed in the high-performance computing cluster at the University of Iowa. The scatter fraction and NECR were calculated by:

$$SF = \frac{Scatter}{Trues + Scatter} \tag{2}$$

and

$$NECR = \frac{T^2}{T + S + k.R} \tag{3}$$

where *T, S,* and *R* are trues, scatter, and randoms coincidence rate, respectively. The scatter fraction is calculated using the true and scatter coincidence events estimated directly in the simulation. Randoms coincidences were measured using the singles-based method. The k value was set to 1 on the assumption that a low variance estimate of randoms is used. Finally, the NECR was computed as a function of activity concentration in the phantom because the PET scanners are often compared based on the peak NECR values. For the comparison of NECR peak values, scanners with rings 4, 8, 20, 30, and 40 were simulated with a scatter phantom of length 200 cm.

i. Simulation using scatter phantom of length 70 cm

The line source was filled with an activity of 1, 2, 5, 10, 20, 40, 60, 80, 100, 200, 300, 400, 500, 600, 700, and 800 MBq ^{18}F, this corresponds to an activity concentration of (0.05 – 36.36) kBq/mL. Scatter phantom volume (~22,000 mL) was used to calculate the activity concentrations.

ii. Simulation using scatter phantom of length 200 cm

The line source in a 200 cm long scatter phantom was filled with an activity of 1, 2, 5, 10, 20, 40, 60, 80, 100, 200, 300, 400, 500, 600, 700, and 800 MBq ^{18}F. Using the phantom volume of ~62,800 mL, the activity concentrations in the phantom were (0.02 – 12.74) kBq/mL.

iii. Count rates curves using NEMA guidelines

First, the GATE simulation output root file's coincidence tree was read in ROOT software[59] to sort the sinogram data, i.e., its *SinogramS* and *SinogramTheta*. The data analysis was then performed in MATLAB for 2D sinogram generations to estimate the trues, randoms, and scatter coincidences. Next, per NEMA[56], the sinogram data were transformed into a 2D histogram with 640 projection bins (-320 to 320 mm from the center of FOV) for the x-axis and 320 bins (0 to π) vertical y-axis. A Gaussian filter was then applied to account for the effect of the detector's limited spatial resolution. Subsequently, the NEMA analysis of Monte Carlo results with randoms from singles rate was performed. An illustration of the NEMA protocols for count rates estimation is shown in **Figure 1**. Once the trues, randoms, and scatters were estimated for different activity levels, the corresponding count rate curves and NECR can be estimated. It should be noted that the same protocols were applied for the extended AFOV scanners as well, although the data were acquired with the extended version of the phantoms.

RESULTS

3.1. Quantification of contribution from Intrinsic Activity from LYSO crystals

The natural radiation from the LYSO crystals have shown only minor impacts on PET imaging performance due to the relatively low energy of gamma emissions from ^{176}Lu decay. The cascaded γ-emissions from ^{176}Lu have energy below the lower DMI scanner energy window threshold as tabulated in **Table 1**. Simulations suggest that in the clinical activity range (5-15 kBq/ml), the impact of the intrinsic activity on count rates is less than 1%; please refer to **Figure 6**. As its impact is statistically low, we did not include the intrinsic activities for all extended LAFOV scanners. In addition, intrinsic activities were not simulated in spatial resolution and sensitivity estimations as it would, in turn, increase the computation cost without impact on results.

2.4. Spatial resolution

Table 2 shows the spatial resolution results in terms of FWHM (mm) for two radial positions in both simulation and measurements. Data show agreement between measured and simulated DMI scanner data, lending confidence to the validity of GATE simulation. The spatial resolution values obtained using the 4-ring simulated scanner model are within (3.20 – 7.97) % of the published measurement results. Simulated FWHMs are consistently demonstrating a better resolution compared to measurement values. It could be due to the absence of modeling within GATE of the process of light spreading and light sharing between the SiPM arrays. The spatial resolution in the center of the transverse field of view is about 4 mm, with an expected radial resolution loss at increased radii.

The transverse resolution, the average of radial and tangential resolutions, at the center of imaging system for different scanner ring configurations is shown in **Figure 2(A)**. Results show that transverse resolution is relatively constant (very small degradation) with extended scanner ring configurations at the center of the scanner FOV. In addition, the results show a degradation in axial resolution when extending the scanner ring configurations up to 30-ring (α ±65º) and a minimal change in axial resolution was found when further extending the scanner to 40-ring (α ±70º). We found that the axial resolution degrades from 4.40 mm to 5.45 mm at the center of the scanner FOV when extending the 4-ring (α ±15º) scanner configuration to 40-ring configuration (α ±70º). In addition, the transverse resolution as a function of position radially offset from the center of the scanner FOV is characterized.

A comparison of transverse resolution between 4, 8, 20, 30, and 40-ring scanner configurations is presented in **Figure 2 (B)**.

The results obtained in this work are similar as the simulation result presented by Schmall et al. using a 4 x 4 x 20 mm^3 LSO crystals.[60] Unlike this work, they simulated the point sources in a warm background in the center of the scanner FOV and they utilized the iterative OSEM algorithm. As this work has followed the NEMA procedures, the results of spatial resolution might have suffered from re-binning and interpolating process of simulated data during the analytic reconstruction.

2.5. Sensitivity

The literature reported sensitivity of the Discovery MI 4-ring scanner was 14.0 cps/kBq [1], while our simulation produced a sensitivity of 14.86 cps/kBq at the center of the field-of-view of the scanner using a 70 cm NEMA sensitivity phantom. This is ~5.95% difference between the measurement and simulation results (**Figure 3A**). The simulated sensitivities using the sensitivity phantom of 200 cm length for 4, 8, 20, 30, and 40-ring scanners were 5.20, 20.84, 109.36, 207.31, and 313.78 cps/kBq respectively. Increase in sensitivity agrees with calculations based on geometry and solid angle. The attenuation-free sensitivities for 4, 8, 20, 30, and 40-ring scanner configurations are presented in **Figure 3 (B)**. **Figure 3 (B)** shows the quadratic (second-order polynomial) increase in sensitivity with axial FOV, as expected.[28] In all simulations, random rates were less than 3%, and scatters were less than 0.5% of the total coincidence events.

It should be noted that sensitivities for 4-ring scanner were simulated using the standard 70 cm long line source for comparison with measurement data. In addition, to suitably compare the sensitivity of 4-ring scanner to extended AFOV scanners, a 200 cm long line source was simulated in

(4 - 40)-ring scanners. Monte Carlo suggests that simulations of 70 cm standard sensitivity phantom in all ring configurations give a sensitivity enhancement up to ~27 times compared to the sensitivity of the 4-ring clinical DMI scanner. Furthermore, sensitivity simulations using a long line source of 200 cm in all scanner configurations performed herein resulted in a sensitivity gain of ~60-fold using a 40-ring scanner compared to the 4-ring scanner. This is illustrated in **Figure 4 (B)**; the area under the axial profile for the 40-ring scanner (red curve) is ~60 times larger compared to the area under the axial profile for the 4-ring scanner (black curve).

The sensitivity profile in the 3D PET was triangular for a 4-ring scanner, as shown in **Figure 4 (A),** with a peak at the center of the field of view, as expected. However, for extended AFOV scanners, sensitivity profiles are no- longer triangular, as shown in **Figure 4 (B),** due to the larger solid angle acceptance. The sensitivity profiles shown in **Figure 4 (B)** will be much different if we simulated a line source in the presence of attenuation medium.[30,61] To understand the impact of attenuation to the sensitivity profiles, a 200 cm long phantom with 30 cm diameter including a line source of 200 cm was simulated for (4-40) ring configurations and the results are presented in **Figure 5**, however, this is not a NEMA test. This is included because the NEMA test does not have the sensitivity test for higher attenuation scenarios as in patient imaging for sensitivity profile comparisons. Sensitivity profiles are relatively uniform in the central 80 cm for 30-ring (1.5 m) scanner and central 120 cm for a 40-ring (2 m) scanner with less than 8% change, as shown in **Figure 5**. This suggests that a single bed position is sufficient for imaging a 80 cm and a 120 cm long object in a 30-ring and 40-ring scanners.[30] The extended AFOV scanners shows the relatively uniform axial profiles at the center of the scanner FOV because the attenuation is greater for oblique lines of response and the center of the scanner FOV contribute more oblique lines of response.[61] This explains the differences in sensitivity between the different ring configurations in almost attenuation free (**Figure 4B**) and higher attenuation (**Figure 5**) scenarios.

2.6. Count rate performance

Count rate results were acquired up to 35 kBq/mL, although clinical FDG studies are typically performed with activity concentrations of less than 15 kBq/mL. Count rates were obtained for the 4-ring scanner using 20 cm diameter 70 cm long phantom are displayed in **Figure 7**. The simulated results included the effects of modeled deadtime. Different types of simulated coincidence count rates as a function of increasing activity concentration are shown in the figure. At first, contributions from crystal's intrinsic activities were estimated by simulating the count rates curve with and without intrinsic activities.

The comparison of simulation with literature measurements resulted in excellent agreement within the measurement uncertainties, in the range of activities practically used in clinical and research scans. The NECR continues to increase slowly beyond the point at which true count rates are equal to the random count rates. For the 4-ring scanner, the measured NECR peak was 201.1 (± 3.14%) kcps at 22.1 (± 3%) kBq/mL with a scatter fraction of 40.4%[1], while the simulated peak NECR was 212.92 (± 2%) kcps at 22.7 kBq/mL with a scatter fraction of 38.9%. Comparing the NECR peak count rates between simulation and measurements gives a percent difference of ~5.71%. It should be noted that the counting rates error at Stanford data[1] was ~3%, and the statistical uncertainties in simulations were < 2.0% for count rate curve estimations. The summary of count rates, scatter fractions and comparisons of NECR peak values for scanners with rings 4, 8, 20, 30, and 40 with a scatter phantom of length 200 cm are plotted in **Figures 8-10**.

We did not find a clear NECR peak within 12 kBq/mL for 20, and 40-ring scanners at the activity concentrations simulated. All simulations are based on a non-paralysable deadtime of 200-ns per detector block. The NECR comparison of 4-ring vs. 40-ring gives a performance enhancement of 28-

fold, whereas comparison of 4-ring vs. 20-ring gives a performance of 15-fold using the 200 cm long scatter phantom in all simulations. The comparison of NECR peak values for 4-40 ring scanners is tabulated in **Table 3**.

3. DISCUSSION

The objectives of this work were to develop a Monte Carlo model of Discovery MI PET scanner and validate its accuracy against published measurement values, and subsequently use this architecture to develop extended AFOV scanner models to study performance. We simulated NEMA tests to characterize the performance of the Discovery MI 4-ring scanner. Subsequently, after validation of a 4-ring Discovery MI scanner, we characterize the performance of extended AFOV scanners, including sensitivity, count rate, and scatter fraction to estimate the sensitivity and NECR gain. LAFOV scanner sensitivity and NECR gain increase significantly with axial length. The NEMA testing of the different ring configurations up to 2 m reveals the performance gain of ~ (28-60) times relative to the 4-ring Discovery MI PET scanner as defined by the sensitivity and NECR peak values.

Validation of the Monte Carlo model of the 4-ring scanner appeared successful. The estimation of spatial resolution was in a close agreement between simulation and measurement data, with less than a 7.97% difference. Spatial resolutions were better in radial and tangential direction than in the axial direction for both the measured and simulated data. Spatial resolution simulations in extended AFOV scanners suggest that the maximum degradation in the axial resolution is ~23.8% compared to the Discovery MI 4-ring scanner. However, the transverse resolution is relatively constant, a very small degradation was observed when increasing the axial acceptance angle up to ±70º. The results obtained in this work compared well with the results presented by Schmall et al.,[60] however the crystal size they used was 4 x 4 x 20 mm^3 (LSO).

A simulated model reproduces the experimental counting rates curves with less than 6% relative errors on the range of clinical activity concentrations found in (2-6 kBq/mL) and less than 8% up to 25 kBq/mL. Also, a comparison of the measured and simulated NECR peak was ~5.71% when comparing the data for the 4-ring scanner. The sensitivity profiles for scanners with AFOV greater than 1 m (20-ring) using the 200 cm long scatter phantom reveals the uniform sensitivity profile at the central part, as shown in **Figure 5**. **Figure 5** tells us that if we want to image major organs, from head to pelvis, with the peak sensitivity then the AFOV of 1.5 m (30-ring) seems sufficient because this configuration shows a relatively uniform profile in the central 80 cm and that covers most of the major organs.

It should be noted that several parameters were not simulated in this study. First, the scanner bed was not considered in this study as its material composition was not known. Second, the crystals' casing materials (light shield) are also not accounted for in simulations as its material and compositions were unknown. The impact of natural radioactivity from LYSO crystals was studied first and found that impact is minimal, < 1%, this is because virtually all the cascaded γ-emissions have energy below the lower threshold of the DMI energy window. Due to this reason, at clinical activity concentrations, background noise from electronics and natural radioactivity from crystals are often considered negligible. Therefore, we did not include LYSO intrinsic activities in all simulations. However, care should be taken when simulating low activity using the extended AFOV scanners and for low count rate imaging applications.

Another limitation of this study is the choice of scanner deadtime in simulations. The dead time digitizer settings have a certain degree of uncertainty since these values were not provided by the manufacturer. The scanner's deadtime was heuristically tuned to match the physical measurements and then applied to other simulations. This could have contributed a few percent in differences between the simulation and measurement results in higher activity concentration simulations. The simulations show a substantial NECR peak enhancement of ~28 times relative to the 4-ring Discovery MI PET scanner for a 2 m long AFOV with 25 mm LYSO crystals thickness. This is aligned with the study performed by Poon et al. using the simulation of the Siemens Biograph mCT with LSO crystals.[29]

These performance enhancements are in-line with those measured on the uEXPLORER[13] and Siemens Biograph Vision Quadra.[14] However, the NECR peak obtained in this work for the 40-ring scanner configuration is about a factor 2 times higher than the NECR peak reported by Spencer et al.[13] using the uEXPLORER scanner. In retrospect, this is not surprising because the LYSO crystal thickness used in uEXPLORER is lower (18.1 mm)[21] than crystals used in Discovery MI geometry (25 mm) and they used a scatter phantom of 175 cm length.[1] The sensitivity of the Discovery MI scanner dramatically decreases, by a factor of (1.30-1.45) when we simulated (4-40)-ring configurations using the crystal thickness of (18.1-20) mm. In addition, the uEXPLORER does not accept all oblique lines of response as they imposed a maximum axial angle of acceptance of ± 57º.[13,21] As the 4-ring DMI scanner uses all oblique lines, we did not restrict the axial angle of acceptance in all extended axial FOV simulations performed herein. This increases the true events however a higher proportion of the oblique events contribute more scatter events, and it increases the attenuation in the scatter phantom **Figures (8-9)**. The scanners used in this work hence collect the data using the maximum axial angle of acceptance of ±15º, ±55º, and ±70º for 4, 20, and 40-ring scanners, as these are the unrestricted acceptance angles for each of these geometries. The NECR peak that we estimated for a 20-ring (1 m) scanner is close to that of uEXPLORER.

The clinical performance of the long axial field of view Biograph Vision Quadra (106 cm) scanner was published.[14] However, their report does not have any suitable data for comparison with this work. Prenosil et al. recently reported the NECR peak of 2.956 Mcps (using maximum full ring difference MRD of 322 with an acceptance angle of ±52º) using Siemens Biograph Vision Quadra[25] which agrees with the simulated NECR peak of 3.066 Mcps using 30-ring DMI scanner as tabulated in **Table 3** in the results section although the NECR peak was obtained at the different activity concentrations.

High sensitivity and extended AFOV PET system would enable short-duration imaging, low-dose imaging[7,62], single bed position scanning, whole-body dynamic and parametric imaging studies[8,9,11,15,63] such as radiotracer kinetics throughout the entire body. This would further enable applications for PET in the field of low count imaging, such as ^{90}Y imaging and theragnostic[64], pediatric imaging[65], screening of patients at risk[66], and possibly many others.[4,5,20]

4. CONCLUSIONS

In conclusion, we modeled the 4-ring Discovery MI PET scanner based on data available in the literature. The simulation models were validated against experimental measurements in the literature using the 4-ring Discovery MI PET scanner. Following the scanner validation, more scanner rings were added to simulate the hypothetical long AFOV scanners up to an axial length of 2 meter. In addition to the standard NEMA NU 2-2018 protocol, a new set of simulations based on extending NEMA phantoms were utilized to characterize the physical performance of the scanners. Spatial resolution, sensitivity, count rates, scatter fraction, and noise equivalent counting rates were evaluated. Overall, the longest AFOV of 2 meter and 25 mm thick LYSO crystals resulted in expected significant performance gains relative to the current 4-ring Discovery MI PET scanner architecture.

ACKNOWLEDGEMENTS

We have benefited from discussions and correspondence with Scott Wollenweber and Chuck Stearns from GE Healthcare. In addition, this research was supported in part through computational resources provided by The University of Iowa. We thank three anonymous reviewers for critically reading the manuscript and their constructive comments.

CONFLICT OF INTEREST

The authors declare to have no conflict of interest to disclose.

DATA AVAILABILITY STATEMENT

Research data of this study are not shared.

REFERENCES

1. Hsu DFC, Ilan E, Peterson WT, Uribe J, Lubberink M, Levin CS. Studies of a Next-Generation Silicon-Photomultiplier-Based Time-of-Flight PET/CT System. *J Nucl Med.* 2017;58(9):1511-1518.

2. Rausch I, Ruiz A, Valverde-Pascual I, Cal-Gonzalez J, Beyer T, Carrio I. Performance Evaluation of the Vereos PET/CT System According to the NEMA NU2-2012 Standard. *J Nucl Med.* 2019;60(4):561-567.

3. van Sluis J, de Jong J, Schaar J, et al. Performance Characteristics of the Digital Biograph Vision PET/CT System. *J Nucl Med.* 2019;60(7):1031-1036.

4. Cherry SR, Badawi RD, Karp JS, Moses WW, Price P, Jones T. Total-body imaging: Transforming the role of positron emission tomography. *Sci Transl Med.* 2017;9(381).

5. Cherry SR, Jones T, Karp JS, Qi J, Moses WW, Badawi RD. Total-Body PET: Maximizing Sensitivity to Create New Opportunities for Clinical Research and Patient Care. *J Nucl Med.* 2018;59(1):3-12.

6. Surti S, Pantel AR, Karp JS. Total Body PET: Why, How, What for? *IEEE Trans Radiat Plasma Med Sci.* 2020;4(3):283-292.

7. Badawi RD, Shi H, Hu P, et al. First Human Imaging Studies with the EXPLORER Total-Body PET Scanner. *J Nucl Med.* 2019;60(3):299-303.

8. Karakatsanis NA, Lodge MA, Tahari AK, Zhou Y, Wahl RL, Rahmim A. Dynamic whole-body PET parametric imaging: I. Concept, acquisition protocol optimization and clinical application. *Phys Med Biol.* 2013;58(20):7391-7418.

9. Karakatsanis NA, Lodge MA, Zhou Y, Wahl RL, Rahmim A. Dynamic whole-body PET parametric imaging: II. Task-oriented statistical estimation. *Phys Med Biol.* 2013;58(20):7419-7445.

10. Dimitrakopoulou-Strauss A, Pan L, Sachpekidis C. Kinetic modeling and parametric imaging with dynamic PET for oncological applications: general considerations, current clinical applications, and future perspectives. *Eur J Nucl Med Mol Imaging.* 2021;48(1):21-39.

11. Rahmim A, Lodge MA, Karakatsanis NA, et al. Dynamic whole-body PET imaging: principles, potentials and applications. *Eur J Nucl Med Mol Imaging.* 2019;46(2):501-518.

12. Zaidi H, Karakatsanis N. Towards enhanced PET quantification in clinical oncology. *Br J Radiol.* 2018;91(1081):20170508.

13. Spencer BA, Berg E, Schmall JP, et al. Performance evaluation of the uEXPLORER Total-body PET/CT scanner based on NEMA NU 2-2018 with additional tests to characterize long axial field-of-view PET scanners. *J Nucl Med.* 2020. doi: 10.2967/jnumed.120.250597.

14. Alberts I, Hunermund JN, Prenosil G, et al. Clinical performance of long axial field of view PET/CT: a head-to-head intra-individual comparison of the Biograph Vision Quadra with the Biograph Vision PET/CT. *Eur J Nucl Med Mol Imaging.* 2021. doi: 10.1007/s00259-021-05282-7.

15. Karakatsanis NA, Zhou Y, Lodge MA, et al. Generalized whole-body Patlak parametric imaging for enhanced quantification in clinical PET. *Phys Med Biol.* 2015;60(22):8643-8673.

16. Karakatsanis NA, Casey ME, Lodge MA, Rahmim A, Zaidi H. Whole-body direct 4D parametric PET imaging employing nested generalized Patlak expectation-maximization reconstruction. *Phys Med Biol.* 2016;61(15):5456-5485.

17. Karakatsanis N, Lodge M, Zhou Y, et al. Novel multi-parametric SUV/Patlak FDG-PET whole-body imaging framework for routine application to clinical oncology. *Journal of Nuclear Medicine 56 (supplement 3) 625.* 2015.

18. Feng T, Zhao Y, Shi H, et al. Total-Body Quantitative Parametric Imaging of Early Kinetics of (18)F-FDG. *J Nucl Med.* 2021;62(5):738-744.

19. Meirelles GS, Erdi YE, Nehmeh SA, et al. Deep-inspiration breath-hold PET/CT: clinical findings with a new technique for detection and characterization of thoracic lesions. *J Nucl Med.* 2007;48(5):712-719.

20. Cherry SR, Badawi RD, Jones T. EXPLORER: Changing the molecular imaging paradigm with total-body PET/CT. *Proc Spie.* 2016;9783.

21. Zhang X, Xie Z, Berg E, et al. Total-Body Dynamic Reconstruction and Parametric Imaging on the uEXPLORER. *J Nucl Med.* 2020;61(2):285-291.

22. Karp JS, Viswanath V, Geagan MJ, et al. PennPET Explorer: Design and Preliminary Performance of a Whole-Body Imager. *J Nucl Med.* 2020;61(1):136-143.

23. Pantel AR, Viswanath V, Daube-Witherspoon ME, et al. PennPET Explorer: Human Imaging on a Whole-Body Imager. *J Nucl Med.* 2020;61(1):144-151.

24. *Siemens Healthineers*. https://www.siemens-healthineers.com/molecular-imaging/pet-ct/biograph-vision-quadra. Accessed March 10, 2021.

25. Prenosil GA, Sari H, Furstner M, et al. Performance Characteristics of the Biograph Vision Quadra PET/CT system with long axial field of view using the NEMA NU 2-2018 Standard. *J Nucl Med.* 2021. doi: 10.2967/jnumed.121.261972.

26. Sui X, Liu G, Hu P, et al. Total-Body PET/Computed Tomography Highlights in Clinical Practice: Experiences from Zhongshan Hospital, Fudan University. *PET Clin.* 2021;16(1):9-14.

27. Viswanath V, Daube Witherspoon ME, Karp JS, Surti S. Numerical observer study of lesion detectability for a long axial field-of-view whole-body PET imager using the PennPET Explorer. *Phys Med Biol.* 2020;65(3):035002.

28. MacDonald LR, Harrison RL, Alessio AM, Hunter WC, Lewellen TK, Kinahan PE. Effective count rates for PET scanners with reduced and extended axial field of view. *Phys Med Biol.* 2011;56(12):3629-3643.

29. Poon JK, Dahlbom ML, Moses WW, et al. Optimal whole-body PET scanner configurations for different volumes of LSO scintillator: a simulation study. *Phys Med Biol.* 2012;57(13):4077-4094.

30. Surti S, Karp JS. Impact of detector design on imaging performance of a long axial field-of-view, whole-body PET scanner. *Phys Med Biol.* 2015;60(13):5343-5358.

31. Zhang J, Knopp MI, Knopp MV. Sparse Detector Configuration in SiPM Digital Photon Counting PET: a Feasibility Study. *Mol Imaging Biol.* 2019;21(3):447-453.

32. Yamaya T, Yoshida E, Inadama N, et al. A Multiplex "OpenPET" Geometry to Extend Axial FOV Without Increasing the Number of Detectors. *Ieee T Nucl Sci.* 2009;56(5):2644-2650.

33. Karakatsanis NA, Zein SA, Nehmeh SA. Evaluation of Image Quality and Quantitation in a Clinical PET Scanner with a Uniformly Sparse Detector Rings Configuration. *IEEE Nuclear Science Symposium and Medical Imaging Conference Proceedings.* 2018. doi: 10.1109/NSSMIC.2018.8824514:1-9.

34. Zein SA, Karakatsanis NA, Issa M, Haj-Ali AA, Nehmeh SA. Physical performance of a long axial field-of-view PET scanner prototype with sparse rings configuration: A Monte Carlo simulation study. *Med Phys.* 2020;47(4):1949-1957.

35. Karakatsanis NA, Zein SA, Nehmeh SA. Positron Emission Tomography with Sparse Block Rings and Continuous Bed Motion. *2019 Ieee Nuclear Science Symposium and Medical Imaging Conference (Nss/Mic).* 2019.

36. Zein SA, Karakatsanis NA, Conti M, Nehmeh SA. Monte Carlo Simulation of the Siemens Biograph Vision PET With Extended Axial Field of View Using Sparse Detector Module Rings Configuration. *Ieee T Radiat Plasma.* 2021;5(3):331-342.

37. Jan S, Santin G, Strul D, et al. GATE: a simulation toolkit for PET and SPECT. *Phys Med Biol.* 2004;49(19):4543-4561.

38. Strul D, Santin G, Lazaro D, Breton V, Morel C. GATE (Geant4 Application for Tomographic Emission): a PET/SPECT general-purpose simulation platform. *Nucl Phys B-Proc Sup*. 2003;125:75-79.

39. Sarrut D, Bala M, Bardies M, et al. Advanced Monte Carlo simulations of emission tomography imaging systems with GATE. *Phys Med Biol.* 2021;66(10).

40. Sarrut D, Bardies M, Boussion N, et al. A review of the use and potential of the GATE Monte Carlo simulation code for radiation therapy and dosimetry applications. *Med Phys.* 2014;41(6).

41. Tiwari A, Graves SA, Sunderland J. The Impact of Tissue Type and Density on Dose Point Kernels for Patient-Specific Voxel-Wise Dosimetry: A Monte Carlo Investigation. *Radiat Res.* 2020;193(6):531-542.

42. Tiwari A, Sunderland J, Graves SA, Strand S, Flynn R. Absorbed dose distributions from beta-decaying radionuclides: Experimental validation of Monte Carlo tools for radiopharmaceutical dosimetry. *Med Phys.* 2020;47(11):5779-5790.

43. Tiwari A, Graves S, Sunderland J. Measurements of dose point kernels using GATE Monte Carlo toolkit for personalized convolution dosimetry. *Journal of Nuclear Medicine.* 2019;60.

44. Allison J, Amako K, Apostolakis J, et al. Recent developments in GEANT4. *Nucl Instrum Meth A.* 2016;835:186-225.

45. Beaudoux V, Blin G, Barbrel B, Kantor G, Zacharatou C. Geant4 physics list comparison for the simulation of phase-contrast mammography (XPulse project). *Phys Med.* 2019;60:66-75.

46. Salvadori J, Labour J, Odille F, et al. Monte Carlo simulation of digital photon counting PET. *EJNMMI Phys.* 2020;7(1):23.

47. Baratto L, Park SY, Hatami N, et al. 18F-FDG silicon photomultiplier PET/CT: A pilot study comparing semi-quantitative measurements with standard PET/CT. *PLoS One.* 2017;12(6):e0178936.

48. *National Nuclear Data Center, NuDat (Nuclear Structure and Decay Data).* https://www.nndc.bnl.gov/nudat2/. Accessed July 30, 2021.

49. Berg E, Zhang X, Bec J, et al. Development and Evaluation of mini-EXPLORER: A Long Axial Field-of-View PET Scanner for Nonhuman Primate Imaging. *J Nucl Med.* 2018;59(6):993-998.

50. Moraes ER, Poon JK, Balakrishnan K, Wang WL, Badawi RD. Towards component-based validation of GATE: Aspects of the coincidence processor. *Phys Medica.* 2015;31(1):43-48.

51. Browne E, Junde H. Nuclear Data Sheets for A=176. *Nucl Data Sheets.* 1998;84(2):337-486.

52. Kossert K, Jorg G, Gostomski CLV. Experimental half-life determination of Lu-176. *Appl Radiat Isotopes.* 2013;81:140-145.

53. McIntosh B, Goertzen AL. Validation of Gate Simulations of the (Lu)-L-176 Intrinsic Activity in Lso Detectors. *Ieee Nucl Sci Conf R.* 2009. doi: Doi 10.1109/Nssmic.2009.5401776:3426-+.

54. Chicheportiche A, Marciano R, Orevi M. Comparison of NEMA characterizations for Discovery MI and Discovery MI-DR TOF PET/CT systems at different sites and with other commercial PET/CT systems. *EJNMMI Phys.* 2020;7(1):4.

55. Wagatsuma K, Miwa K, Sakata M, et al. Comparison between new-generation SiPM-based and conventional PMT-based TOF-PET/CT. *Phys Medica.* 2017;42:203-210.

56. *NEMA NU 2-2018 Performance Measurements of Positron Emission Tomograph (PET).* Rosslyn, VA2018.

57. Thielemans K, Tsoumpas C, Mustafovic S, et al. STIR: software for tomographic image reconstruction release 2. *Phys Med Biol.* 2012;57(4):867-883.

58. Schindelin J, Rueden CT, Hiner MC, Eliceiri KW. The ImageJ ecosystem: An open platform for biomedical image analysis. *Mol Reprod Dev.* 2015;82(7-8):518-529.

59. Brun R, Rademakers F. ROOT - An object oriented data analysis framework. *Nucl Instrum Meth A.* 1997;389(1-2):81-86.

60. Schmall JP, Karp JS, Werner M, Surti S. Parallax error in long-axial field-of-view PET scanners-a simulation study. *Phys Med Biol.* 2016;61(14):5443-5455.

61. Daube-Witherspoon ME, Viswanath V, Werner ME, Karp JS. Performance Characteristics of Long Axial Field-of-View PET Scanners with Axial Gaps. *IEEE Trans Radiat Plasma Med Sci.* 2021;5(3):322-330.

62. Zhang YQ, Hu PC, Wu RZ, et al. The image quality, lesion detectability, and acquisition time of (18)F-FDG total-body PET/CT in oncological patients. *Eur J Nucl Med Mol Imaging.* 2020;47(11):2507-2515.

63. Fahrni G, Karakatsanis NA, Di Domenicantonio G, Garibotto V, Zaidi H. Does whole-body Patlak F-18-FDG PET imaging improve lesion detectability in clinical oncology? *Eur Radiol.* 2019;29(9):4812-4821.

64. Wright CL, Zhang J, Tweedle MF, Knopp MV, Hall NC. Theranostic Imaging of Yttrium-90. *Biomed Res Int.* 2015;2015:481279.

65. Zhao YM, Li YH, Chen T, et al. Image quality and lesion detectability in low-dose pediatric (18)F-FDG scans using total-body PET/CT. *Eur J Nucl Med Mol Imaging.* 2021;48(11):3378-3385.

66. Lennon AM, Buchanan AH, Kinde I, et al. Feasibility of blood testing combined with PET-CT to screen for cancer and guide intervention. *Science.* 2020;369(6499).

Figure 1: Count rates estimation using the NEMA protocol.[56] The activity of 800 MBq was used in the scatter phantom to generate this figure using the 4-ring scanner. (A) Sinograms of coincidences obtained from GATE root output (B) Sinogram after inserting Gaussian filter and setting pixels farther than 12 cm from the center of FOV to zero (C) Sinogram after alignment according to maximum values for each projection angle (D) Sum of all projection angles of the sinogram (E) Selecting the central 40 mm strip to estimate the scatters and randoms (F) plot of count rates curves and NECR. A sinogram-based analysis was performed to estimate the coincidence event rates.

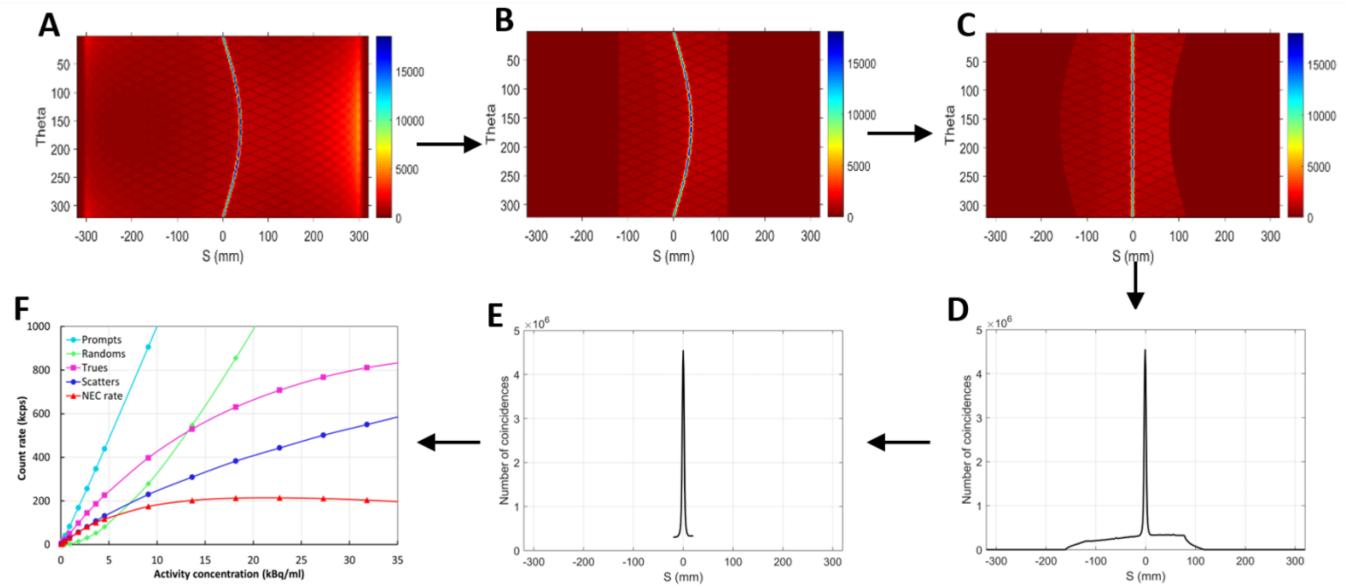

Figure 2: (A) Spatial resolution along the axial and transverse (average of radial and tangential) direction for different scanner rings (B) Transverse resolution for six-point sources with varying radial offsets (at 0, 1, 5, 10, 15, and 20 cm) in the center of the axial FOV for five scanner geometries.

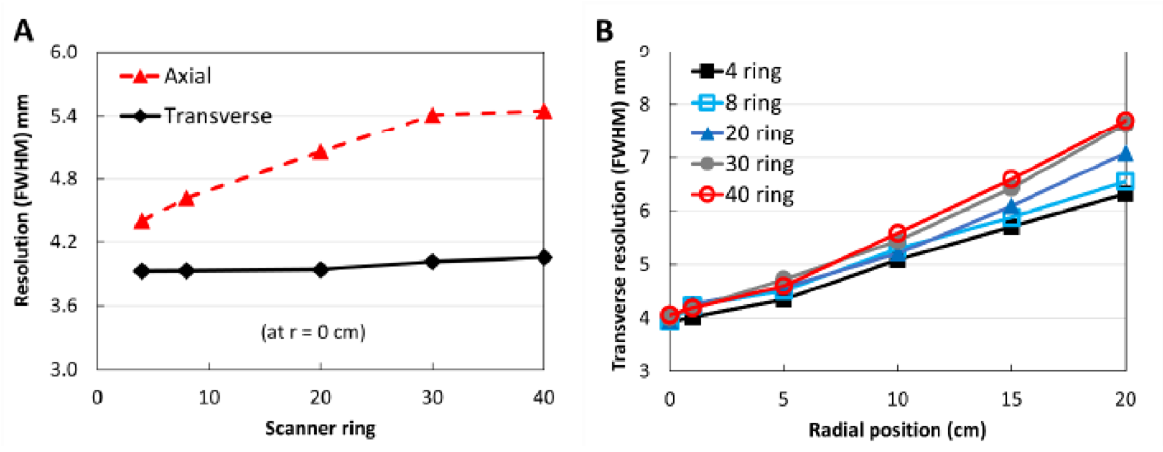

Figure 3: (A) Figure shows a comparison of simulated and measured absolute attenuation free sensitivity for the DMI 4-ring scanner. There is a 6.41% difference between simulation and measurement[1] data points. Exponential regression of the true count rates was used for attenuation-free sensitivity estimation. (B) Comparison of attenuation-free sensitivities for 4, 8, 20, 30, and 40-ring scanners.

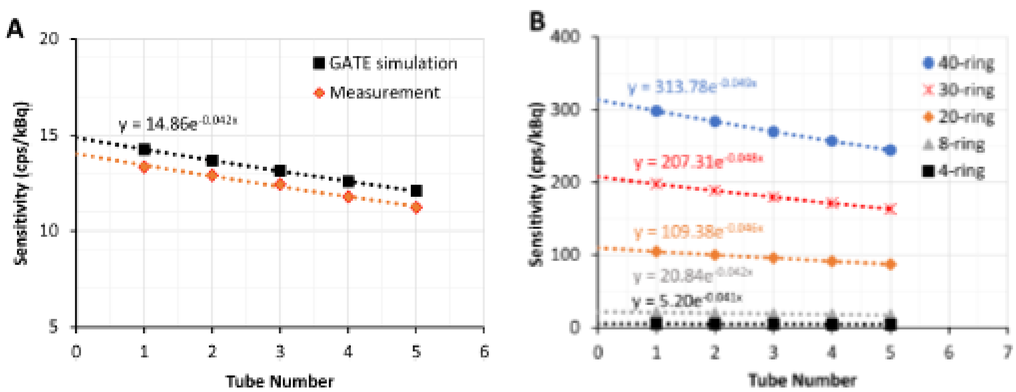

Figure 4: (A) Axial sensitivity profile of contiguous axial slices from the center of the scanner for 4-ring scanner. (B) Axial sensitivity profiles for 4, 8, 20, 30, and 40-ring scanner configurations. Acceptance angles were not restricted for these profiles as the Discovery MI scanner accepts all oblique lines. Sensitivity profiles were obtained using simulation of a 200 cm long 3.2 mm diameter line source with 4 MBq ^{18}F activity.

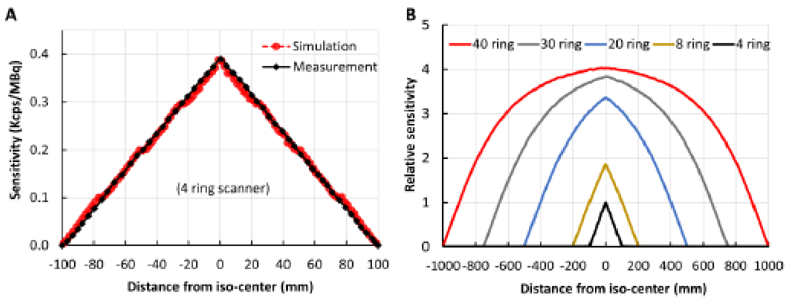

Figure 5: Relative sensitivity profiles for a line source of 200 cm length in a 30 cm diameter, 200 cm long cylindrical phantom, for scanners with 4-ring, 8-ring, 20-ring, 30-ring, and 40-ring configurations. Line source had a same diameter as in NEMA sensitivity phantom. Similar sets of sensitivity profiles were seen in simulations performed by Surti et al.[6]

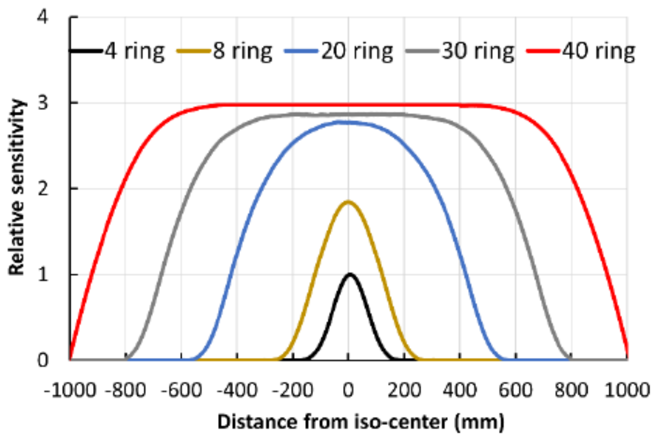

Figure 6: Count rates comparison between simulation with and without intrinsic activities (IA). The volume of the scatter phantom was considered for the activity concentration calculations. The impact of intrinsic activities was found to be < 1% in the clinical activity range. Therefore, intrinsic activities in LYSO crystals are not included in all simulations performed herein to save the computation burden.

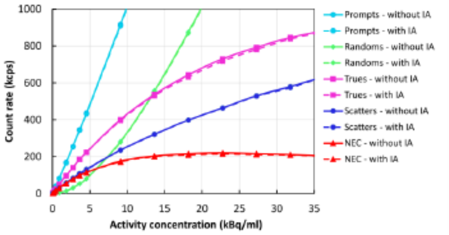

Figure 7: Comparison of count rates curve between simulation and measurement performed at Stanford University for DMI 4-ring scanner.[1] The volume of the scatter phantom (~22 L) was considered for the activity concentration calculations. The maximum deviation in activity concentration measurements was 2.43%.

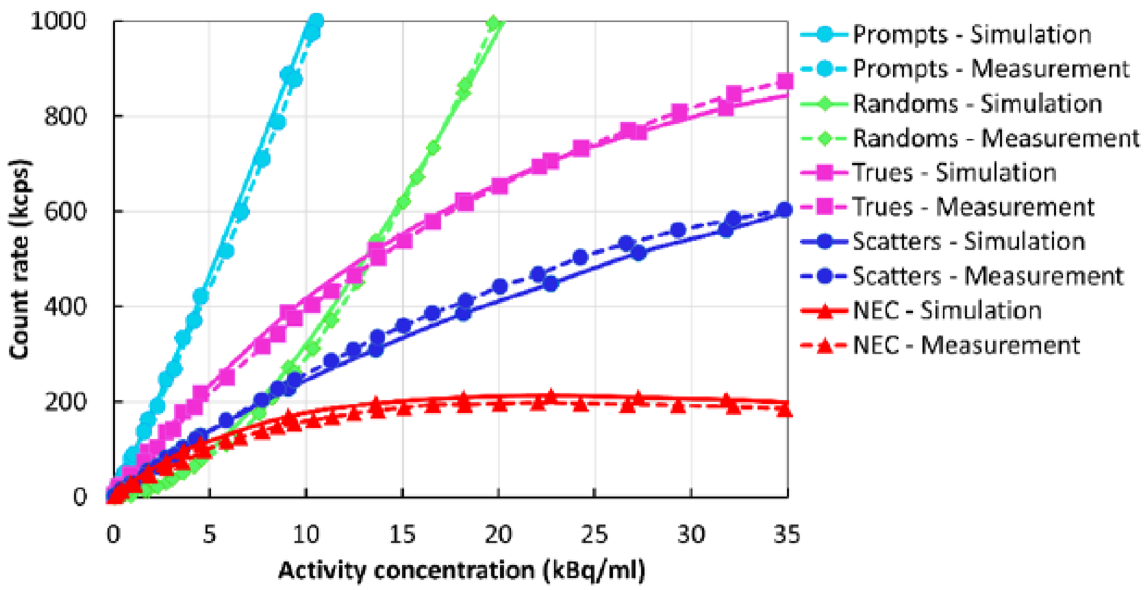

Figure 8: Count rate curves and NECR for 4-ring (AFOV 20 cm) and 20-ring (1 m AFOV) scanner. Count rate curves for the 4-ring scanner lies at the bottom of the plot. For comparison with 4 and 20 ring scanner NECR, a 200 cm long scatter phantom was simulated in both ring configurations. A gain of 15 times can be expected when comparing the NECR peak values.

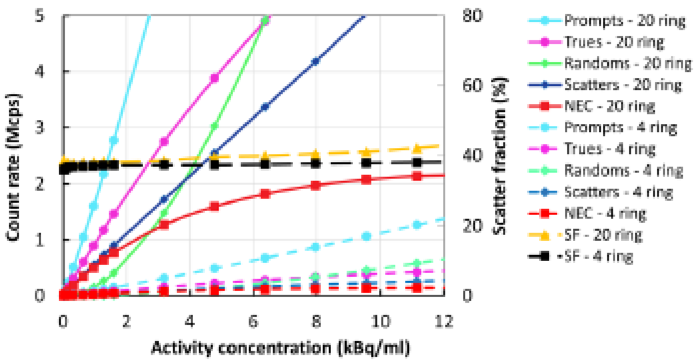

Figure 9: Count rate curves and NECR for 4-ring (AFOV 20 cm) and 40-ring (2 m AFOV) scanner. Count rate curves for the 4-ring scanner lies at the bottom of the plot. For comparison, 200 cm long scatter phantom was simulated in both ring configurations. A gain of 28 times can be expected when comparing the NECR peak values.

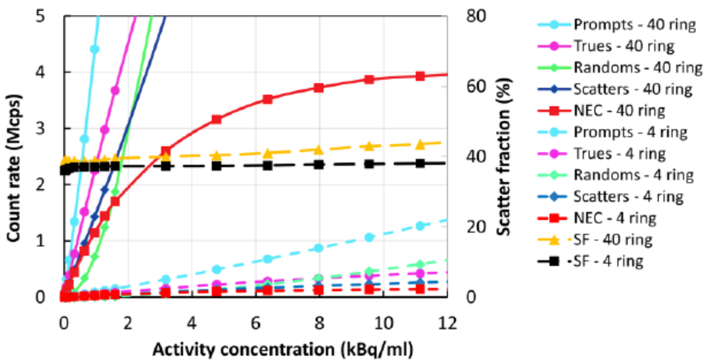

Figure 10: The increase in NECR as a function of axial length for 4, 8, 20, 30, and 40-ring scanners. Note that for this comparison, all scanners were simulated with 200 cm long scatter phantom with an activity concentration range of (0.02 – 12.74) kBq/mL.

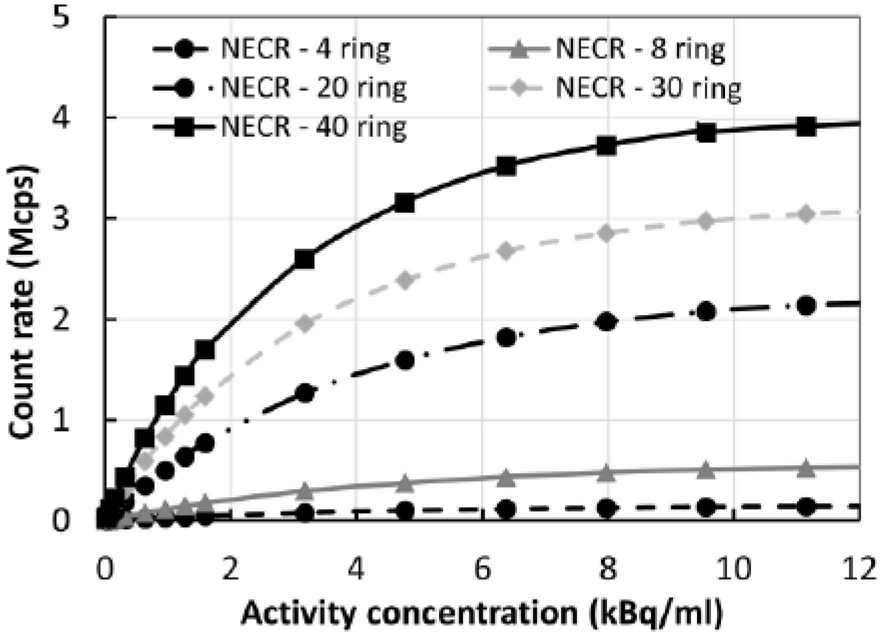

Table 1: Specifications of the Discovery MI used in the simulation for 4-ring scanner.

Crystal material	LYSO
Number of major rings	4
Axial crystal rings	36
Transaxial crystals per ring	544
Size of crystals (mm^3)	3.95 × 5.3 × 25
Total number of crystals	19,584
Axial FOV (mm)	200
Bore diameter (mm)	700
Coincidence window width (ns)	4.9
Energy resolution	12% at 511 keV
Timing resolution (ps)	375

Lower energy threshold (keV)	425
Upper energy threshold (keV)	625

Table 2: Spatial resolution results for different radial, tangential and axial positions for simulated and measured point sources at two radial positions: (0, 1, 0) cm and (0, 10, 0) cm within the scanner FOV. The mean values of the three different reconstructed images are reported. Measurement performed at Stanford University from Hsu et al.[1] are also reported for comparison.

	GATE simulations (this work)		**Measurement (Stanford)[1]**	
	FWHM	FWTM	FWHM	FWTM
(0, 1, 0) cm				
Radial	3.94	8.87	4.17	9.14
Tangential	4.10	8.68	4.40	9.17
Axial	4.41	9.79	4.57	10.38
(0, 10, 0) cm				
Radial	5.29	9.78	5.65	10.36
Tangential	4.89	9.24	4.74	9.68
Axial	5.90	11.52	6.39	12.34

Table 3: Comparison of NECR peak values for 4 - 40 ring scanners. The NECR peak value for 4-ring scanner using a 200 cm long scatter phantom is compared to 8, 20, 30, and 40-ring scanner configurations.

	NECR peak (Mcps)	NECR Gain
4 - ring	0.143	1
8 - ring	0.536	3.75
20 - ring	2.162	15.12
30 - ring	3.066	21.44
40 - ring	3.975	27.80